Studying phase change memory devices by coupling scanning precession electron diffraction and energy dispersive X-ray analysis

Loïc Henry, Nicolas Bernier, Martin Jacob, Gabriele Navarro, Laurent Clément, Jean-Luc Rouvière, Eric Robin

Version of Record: https://www.sciencedirect.com/science/article/pii/S1359645420307278
Manuscript_f6540a778a74ae3967980d2df8c7bd85

Studying Phase Change Memory devices by coupling Scanning Precession Electron Diffraction and Energy Dispersive X-ray analysis

Loïc Henry (corresponding author)
loic.henry@cea.fr
+33 4 38 78 55 62
STMicroelectronics, 850 Rue Jean Monnet, 38920 Crolles, France
Univ. Grenoble Alpes, CEA, LETI, F-38000 Grenoble, France

Nicolas Bernier
nicolas.bernier@cea.fr
Univ. Grenoble Alpes, CEA, LETI, F-38000 Grenoble, France

Martin Jacob
martin.jacob@cea.fr
Univ. Grenoble Alpes, CEA, LETI, F-38000 Grenoble, France

Gabriele Navarro
gabriele.navarro@cea.fr
Univ. Grenoble Alpes, CEA, LETI, F-38000 Grenoble, France

Laurent Clément
laurent-renaud.clement@st.com
STMicroelectronics, 850 Rue Jean Monnet, 38920 Crolles, France

Jean-Luc Rouvière
jean-luc.rouviere@cea.fr
Univ. Grenoble Alpes, CEA, IRIG, F-38000 Grenoble, France

Eric Robin
eric.robin@cea.fr
Univ. Grenoble Alpes, CEA, IRIG, F-38000 Grenoble, France

Abstract

A new simultaneous acquisition software for Precession Electron Diffraction (PED) and Energy Dispersive X-ray Spectroscopy (EDX) mapping has been developed. This approach has been used to study the RESET operation in Ge-rich Ge-Sb-Te (Ge-rich GST) non-volatile Phase-Change Memory (PCM). Such an operation consists in the local amorphization of the device's active volume, which defines the memory state. Using PED patterns indexing, we were able to segment the amorphous area, and access its composition through EDX quantification. Moreover, both the spatial distribution and the chemical composition of the two crystalline phases overlapped in the chalcogenide layer were retrieved by using the spectral unmixing approach and PED patterns indexing. It evidences that Ge and $Ge_2Sb_1Te_2$ (GST-212) crystals are separated in the studied devices. Despite this, we show that Ge-enrichment is preserved in the active volume of a functional device, which is crucial to

guarantee the RESET state stability at high temperature. We also link the origin of the failure of the RESET operation observed in a dysfunctional device to the larger Ge-depleted area.

Keywords: EDXS; Electron diffraction pattern; Phase Change Memories; Spectral decomposition; Transmission Electron Microscopy

Introduction

In the last two decades, Phase-Change Memory (PCM) technology has shown outstanding progress. In a general context marked by the need of a next-generation of Non-Volatile Memory (NVM) [1], Ge-Sb-Te (GST) based PCM has proven its reliability in terms of scalability [2], programming speed [3] and endurance [4]. PCM is considered as the most mature memory technology among the emerging ones, and it can be applied in both embedded and stand-alone systems.

Among the stable compositions investigated along the Sb_2Te_3-GeTe tie-line, $Ge_2Sb_2Te_5$ has been intensively studied for its advantageous tradeoff between crystallization speed and activation energy [5]. However, its low crystallization temperature of about 170 °C is not compatible with embedded automotive applications, requiring stability for several years at 150 °C. With the aim of improving stability at high temperature, Ge-enrichment [5], and nitrogen or carbon doping have been proposed [6-8]. Later on, an optimized Ge-rich Ge-Sb-Te (Ge-rich GST), referred as T-alloy, has been presented [9] for automotive market applications. This optimized alloy fits the challenging automotive specifications, ensuring both code integrity and data retention in high temperature environments. Integrating this Ge-rich GST alloy into state-of-the-art PCM, an innovative 28 nm FD-SOI e-NVM technology for automotive application has recently been presented [10]. In such devices, the control of GST stoichiometry is crucial in order to accurately meet the strict target requirements. Ge-rich GST refers to the “as-deposited” composition which is amorphous and homogenous. However, during annealing of full sheet deposited layers, a phase separation between Ge and a GST phase occurs [9, 11-13], leading to chemical and crystalline modifications. That could appear as well during the Back-End-Of-Line (BEOL) process fabrication, which consists in a standard CMOS integration process. Moreover, composition variations in the active region of the PCM cell have been reported after activation operation [14, 15] and cycling [16], due to local Ge migration. If such mechanism were to trigger a failure in standard Ge-Sb-Te alloys [17-19], it is intrinsic and necessary in Ge-rich GST for the functionality of the device.

In this study, we focus on the understanding of the origin of the extrinsic RESET programming failure of a Ge-rich GST based PCM device after BEOL process. To do that, we have characterized both structure and chemistry of GST wall-structure PCM devices [2] used in 28 nm FDSOI e-NMV technology developed by STMicroelectronics [10]. We applied the Automated Crystal Orientation and phase Mapping technique developed for Transmission Electron Microscopy (ACOM-TEM), also known as ASTAR. This technique was used for the characterisation of phases, while EDX was applied for chemical quantification of both crystalline and amorphous phases. Through the use of a simultaneous PED/EDX acquisition, we report the benefits of an exact correlation between both datasets.

2. Material and Methods

2.1 Material

A scheme of the PCM stacking with a sectional view of the structure is shown in **Fig. 1**. The active device is built on a stack comprising, from bottom to top, a silicon substrate, a 25 nm-thick buried oxide, a <100> orientation Si thin film and a tungsten bottom electrode. The bottom electrode is connected to the GST layer by a thin TiN element, named "heater". This conductive material is deposited by etching into an insolent silicon nitride layer, and allows to obtain a localized Joule heating of the GST. We remind that PCM relies on the transition between an amorphous resistive state (RESET state) and a crystalline conductive state (SET state) of a small volume of GST above the heater. Both RESET and SET programming are achieved by applying adequate current pulses. On the top of the device, a 20 nm-thick TiN encapsulation layer is deposited onto the chalcogenide layer.

The first RESET programming operation of the PCM includes an initial activation procedure, also named "forming" operation. It allows to switch the cell from a highly resistive virgin state to a lower and suitable resistive state for embedded memory application [14, 15]. Such operation leads to the formation of a conductive path between the heater and the top electrode, along which the material gets melted. This melted area then constitutes the programming region of the cell, also called active area. At the end of the BEOL process fabrication, the PCM test vehicle is submitted to a high temperature bake in order to explore the RESET programming reliability after extreme BEOL conditions. We remind that we focus our analyses on two cells, one programmed successfully in the RESET state (RESET-Pass), and the other failing at the RESET programming (RESET-Fail) being its resistance below the target one (i.e. 1MΩ). We analysed a region on interest on each cell (**Fig. 1**).

2.2 Experimental techniques

The sample was prepared along the bit-line direction by Ga^+ Focused Ion Beam (FIB) milling using a FEI Helios 450 machine. A tungsten protection layer was deposited to protect the two regions of interest from the tails of the ion beam and the specimen was deposited onto a molybdenum TEM grid. Then, we used a 30 kV operation voltage for the initial thinning and finished with a low beam energy in the range 5-8 kV to reduce FIB-induced damage. Both cells were observed at 200 kV using a probe corrected Titan Themis FEI microscope equipped with the Super-X detector system for Energy Dispersive X-ray (EDX) spectrometry and a Gatan US1000 CCD camera for diffraction patterns acquisition. The Super-X system comprises four 30mm² windowless silicon drift detectors placed at an elevation angle of 18° from the horizontal with a symmetrical distribution along the beam axis (45°, 135°, 225° and 315° azimuthal angles) and a 0.64 ± 0.06 sr total solid angle [20]. EDX was used for chemical characterization whereas ASTAR [21] technique was used to automatically index diffraction patterns for phase identification.

Simultaneous acquisition of EDX spectrum and diffraction patterns was performed in precession mode (PED-EDX) using a homemade Digital Micrograph (DM) script. This script synchronizes (i) the beam shift between the acquisition points and the collection of (ii) the diffraction patterns and (iii) the EDX spectra, while the precession is activated using the precession option available in the user interface of the microscope. It only differs from Scanning Precession Electron Diffraction in that EDX spectra are collected simultaneously

with the diffraction patterns. Note that, by performing a simultaneous PED-EDX acquisition, we ensure that the datasets have an exact pixel correlation. Hence, it allows an accurate correlation between the structure and the composition. A schematic of the simultaneous acquisition and datasets is shown in **Fig. 2**.

The TEM was used in microprobe mode with a gun lens of 1, a spot size of 4, a 30µm C_2 aperture, a probe current of 150-200 pA and a precession angle of 0.5°. Considering the Full Width at Half Maximum (FWMH), we measured an electron probe size of 4.0 nm on a monocrystalline [110]-oriented silicon of a 100-nm thick lamella. We also determined a beam convergence semiangle of 1.2 mrad using a diffraction pattern obtained on the same [110]-oriented silicon. **Fig 1b** presents a TEM image showing the two acquisition areas, one on the RESET-fail cell and one on the RESET-Pass cell. Both cells were scanned over a 102 x 92 nm² area using a 2.6 nm pixel size and a 0.9 s dwell time. For each acquisition, both diffraction patterns and EDX spectra were recorded as 40 x 36 pixel images.

2.3 Data analysis

Ge K-, Sb L- and Te L-lines were extracted from EDX spectra using the Kramer background subtraction method implemented in Gatan Microscopy Suite 3 (GMS 3). The k-factors were determined for GST quantification using the theoretical expression of k_{ij}, the k-factor of element i relative to element j:

$$k_{ij} = \frac{M_i}{M_j}\frac{Q_j\omega_j\alpha_j}{Q_i\omega_i\alpha_i}\frac{\varepsilon_j}{\varepsilon_i}$$

Where $M_{i,j}$ are the atomic masses, $Q_{i,j}$ are the ionization cross-sections (cm^2), $\omega_{i,j}$ are the fluorescence yields, $\alpha_{i,j}$ are the relative intensities of the X-ray lines for elements *i* and *j*, and $\varepsilon_{i,j}$ are the detection efficiencies for these lines. Using the net X-ray intensities of the Ka+Kb and La+Lb+Lg lines for GST quantification, k-factors were determined relative to silicon with $\alpha_{i,j}$=1. From the NIST database [22], the total emission cross sections ($Q.\omega$) were evaluated at 9.34×10^{-23} cm², 19.01×10^{-23} cm², 19.09×10^{-23} cm² and 8.46×10^{-23} cm² for the Ge K-, Sb-L, Te-L and Si-K lines, respectively. We assumed an Al contact and a Si dead layer of 30 nm each to evaluate the detector efficiency at 96%, 99%, 99% and 97% for the Ge K- Sb L-, Te L- and Si-K lines, respectively. Therefore, the theoretical k-factors are 2.36, 1.89 and 1.97 for the Ge K- Sb L- and Te L-lines, respectively.

The two EDX maps, obtained on the RESET-Pass and RESET-Fail cells, were combined into one to increase the number of spectra for statistical analysis. The acquisition conditions being the same, we were able to concatenate the two images into a single dataset. Note that this operation is not possible in case EDX acquisition conditions are varying as it would result in non-comparable datasets and then an incorrect statistical analysis.

Using the open source Hyperspy toolbox [23], scikit-image [24] and sci-kit-learn packages [25], Principal Component Analysis (PCA) was applied as a denoising method with a weighting pre-treatment for Poisson noise normalization on the merged datasets [26]. This method consists in identifying the components that yields most of the variance of the data, and hence meaningful information, separating them from noise. The PCA scree plot was used to determine the number of components that explains most of the variability in the dataset. Six components were found, which is in agreement with the five expected chemical phases (titanium nitride, silicon nitride, silicon oxide, GST and Ge), plus the EDX zero peak

frequency detected as a component.
We then used Spectral Unmixing techniques to express the spectrum in each pixel of our images as a linear combination of a given number of spectral endmembers. We used Vertex Component Analysis (VCA) [27], to extract the spectral signatures of five components present in the data. This approach differs from other multivariate statistical analysis already used for EDX data such as Independent Components Analysis (ICA) [28], or Non-negative Matrix Factorization (NMF) [29], because VCA have a pure-pixel hypothesis ensuring that the extracted components are present in the original data. In our case, the five components considered as pure pixels were in agreement with the five expected chemical phases mentioned above. We then used the Sparse Unmixing by variable Splitting and Augmented Lagrangian (SUNSAL) algorithm [30] to estimate their abundance fractions. Both VCA and SUNSAL algorithms were performed using the python implementation proposed here [31].

Finally, the diffraction patterns were acquired and converted to the blockfile format of the ASTAR software without applying any filter. Based on XRD analysis, two crystalline phases were identified to characterize the chalcogenide layer: the Ge cubic phase (space group n°227) and the $Ge_2Sb_2Te_5$ cubic phase (space group n°225). We generated $Ge_2Sb_2Te_5$ from XRD observations realized on the bulk sample, also reported in [19], and in agreement with [9, 32] (Table 1). Camera length for ASTAR indexation was calibrated using the silicon substrate.

	a, b, c (nm)	*A, β, γ (deg)*	*Space group*	*Laue Class*
Ge	5.650	90	f d 3 m	m-3m
GST	6.027	90	f m 3 m	3-3m

Table 1: Parameters used for ASTAR theoretical templates creation. For Ge we used Crystallographic Information File (CIF) ID 9008567, while for $Ge_2Te_2Te_5$ the CIF file was generated from XRD observations reported in [19], and in agreement with [9, 32].

3. Results

Fig. 1b shows a standard High-angle Annular Dark-field (HAADF) image of the RESET-Fail (on the left) and RESET-Pass (on the right) cells. Such images, based on the collection of incoherently scattered electrons at high angles, are very sensitive to mass thickness variations (Z-contrast) [33]. Within the GST layer, we observe multiple contrast variations which are likely to reveal an inhomogeneous chemical distribution. Such variations are compatible with either the phase separation mechanism described in Ge-rich GST materials [12] or the void formation observed in [7]. However, both chemical and structural information are required to distinguish between these two mechanisms.

Fig. 3a-c show an example of the template matching method of the ASTAR indexing, which consists in correlating the recorded PED patterns with simulated templates [21]. The ASTAR correlation index (Q) reflects the degree of matching. We present here an example of PED pattern recorded on the RESET-Fail device and its indexation according to the $Ge_2Sb_2Te_5$ template (correlation index Q = 833). Note that, on the same diffraction pattern, the Ge template has a much lower correlation index (correlation index Q = 492). Despite the structures similarities between Ge and GST structures, we show that phase identification can be achieved with a comfortable percentage difference of the matching indexes (41%), which

is the best parameter to estimate the reliability of the indexing [21]. Usually, values above 15% are sufficient to confirm the validity of the detected phase [21]. **Fig. 3a-c** also illustrate the importance of using precession to extend the visible reflections on the collected diffraction patterns. Due to Ge and GST structures similarities, the presence of high-order reflections is crucial to enable a reliable pattern indexing.

Fig. 4a presents the ASTAR index correlation map obtained on the RESET-Pass cell. Firstly, we observe an amorphous dome located above the TiN heater. Indeed, diffraction patterns extracted from this area (see inset in **Fig. 4b**) present characteristic halo ring patterns revealing an amorphous material. Thus, **Fig. 4a** enables to measure a dome diameter of 8 ± 2 nm. Note that crystalline phases are likely to partially cover the amorphous area, leading to an underestimation of the dome size.
In order to better highlight the chemical and morphological aspects of the amorphous dome, **Fig. 4b** shows a view overlapped with the STEM-EDX hyperspectral map. To segment the active dome, ASTAR correlation index was used to distinguish amorphous from crystalline areas. Indeed, as halo ring patterns do not match Ge and GST templates, both correlation indices are low (≤ 50). Then, an X-rays intensities-based mask was applied to extract the amorphous GST dome from the amorphous nitride, as summarised in the schematic flow chart in **Fig. 2**. **Fig. 4c** shows the results of the amorphous dome spectra quantification. We observe that the compositions remain close to the Sb_2Te_3-Ge tie-line which is investigated in the frame of high thermal stability GST development by increasing the Ge content in GST materials [5, 34]. Such Ge-rich GST alloys, dedicated to achieve the automotive market requirement [34], are the ones of interest in this study. Hence, the agreement between the type of Ge-rich alloy studied and the composition displayed in **Fig. 4c** supports the quantification reliability. Due to grains overlapping along the lamella thickness [35, 36], this method could not be applied to determine the GST phase stoichiometry. Indeed, since the EDX signal is averaged by the grain distribution in each pixel, the spectra recorded are combinations of Ge and GST signals which have to be unmixed for proper GST phase stoichiometry determination. This spectral unmixing step, performed using VCA, is described in the following section.

Fig. 5 shows the five endmembers signatures extracted by VCA and their abundance maps in insets. As mentioned, the number of components chosen is in agreement with the scree plot and the number of phases expected in the acquisition area (**Fig. 1**). Then, by comparing spectral signatures, abundance maps and device architecture (**Fig. 1**), endmembers can be clearly identified. Endmembers 3, 4 and 5 corresponds to titanium nitride, silicon nitride and silicon oxide, respectively. Endmembers 1 and 2, which are distributed in the GST layer, can be identified as GST and Ge pure phases, respectively. No significant Sb L- nor Te L-lines are observed in endmember 2 spectral signature, indicating that pure Ge crystal phases are present, as shown by XRD results. The same GST phase is found in both RESET-Pass and RESET-Fail cells, showing that no difference in the stoichiometry is detected. VCA was also performed on both datasets separately to confirm that the same GST stoichiometry was found.

In each spectral signature Si K-, N K-, Mo L- and Cu K-lines are visible. Firstly, it is known that X-ray emission from the pole piece of the microscope and the specimen holder causes Mo L- and Cu K-lines. Moreover, the silicon nitride which surrounds the cells cannot be completely removed during FIB milling without deteriorating the device (as shown in 3D architecture reported in [10]). Hence, a thin amorphous silicon nitride layer remains on both

sides of the TEM lamella, producing the Si K- and N K-lines in each EDX spectrum. However, as this layer distribution is homogeneous along the studied areas (no more components are detected by PCA), it has no influence on the endmembers extraction. The estimate of the GST phase composition, shown in **Fig. 5a,** was determined by quantifying the spectra with more than 90% of the highest abundance of GST phase. Taking into account the uncertainties related both to the statistical uncertainty and the use of theoretical k-factors, the composition measured is compatible with $Ge_2Sb_1Te_2$ (GST-212) [6]. **Fig. 5e** displays, in a ternary plot, both experimental GST and GST-212 phases. It should be noted that a larger statistical sample would be required to definitely confirm the GST stoichiometry found. A larger scanned area would provide such a large statistical sample, but it was not performed in this study.

Fig. 6a-b show the index correlation and ASTAR phase maps obtained on the RESET-Pass cell. We first observe that, despite the Ge and GST structures similarities, both phases are detected. Thereby, this result is in agreement with the XRD analysis and the phase separation described in Ge-rich GST materials [12]. Also, comparing ASTAR phase map to abundance maps of both GST and Ge endmembers presented in **Fig. 6c-d**, a good agreement can be observed.
Fig. 6e-f show the index correlation and ASTAR phase maps obtained on the RESET-Fail cell. As in **Fig. 6b**, Ge and GST grains are detected within the polycrystalline GST layer. However, we notice that a larger GST grain is located above the titanium nitride heater with respect to previous analysis, and that a lower Ge abundance is measured in this area with respect to the active volume of the RESET-Pass cell. Thus, the active area of the RESET-Fail cell shows a composition closer to GST-212. Also, the GST layer either contains an amorphous dome too small to be detected or it remains fully crystalline. In both cases, this observation corroborates the low resistance value measured for the RESET-Fail cell.
Despite disagreements for a few pixels between ASTAR and VCA results, the phase indexed by ASTAR is detected as the most abundant by VCA in most cases. We thus observe an excellent agreement by comparing the ASTAR phase with the VCA abundance maps**.** It supports that, despite structure similarities and grains overlapping, ASTAR indexation and VCA unmixing provide reliable results. Note that more details can be found in the Supplementary Information accompanying this contribution. All these experimental results are discussed in the following section.

4. Discussion

Fig. 7 summaries the main findings of our study. It displays (i) the GST crystalline stoichiometry found by VCA for both cells, (ii) the amorphous dome composition of the RESET-Pass cell, calculated by taking the average of compositions shown in **Fig. 4c**, and (iii) the composition of the RESET-Fail cell active area occupied by the large GST grain. While the core volume of the RESET-Fail cell is occupied by a large GST-212 grain, the GST-212 phase is enriched in Ge-content in the active volume of the RESET-Pass cell.

We remind that, as explained in [14, 15], the activation procedure allows to switch the cell from a highly resistive virgin state towards a steady working state. This operation, based on the atomic reorganization that takes place in the active volume of the cell during the

activation process, is responsible for the PCM cell reversible and non-volatile resistance state transitions. It leads to the formation of a conductive path between the heater and the top electrode, causing the Ge migration towards the periphery of the melted volume. This half-dome shaped area, visible in **Fig. 6d,** is the active region of the cell. The higher content in Ge with respect to GST-212 phase found in the amorphous active volume, demonstrates the capability of the cell to feature a higher retention temperature with respect to standard GST-212, required to satisfy automotive specifications. Indeed, an alloy with such Ge-enrichment has a crystallisation temperature higher than 250 °C [15].

VCA results show that the same GST crystalline phase stoichiometry is found in both RESET-Pass and RESET-Fail cell. However, we can observe that its spatial distribution is different in the two cases. The RESET-Pass cell exhibits multiple fine GST and Ge grains, and an amorphous Ge-rich GST-212 core volume, while the RESET-Fail cell shows a large GST-212 grain above the heater which occupies the majority of the acquisition area. This result confirms that the properties of Ge-rich GST materials do not result from a specific crystallographic phase but from atomic diffusion [11], and the spatial distribution of the different phases in the microstructure.

The GST grain formation observed in the RESET-Fail cell, which also corresponds to a larger Ge-depleted volume with respect to RESET-Pass cell, is compatible with an "overshoot" phenomenon. This phenomenon likely happened during the activation operation, when the cells are gradually activated with a staircase up programming voltage [15]. We think that the presence of a region particularly rich in Ge content or containing a pure Ge grain above the heater would require a higher voltage during the activation step with respect to a standard cell. Such a Ge enriched region likely remained after the partial segregation of the Ge-rich GST alloy triggered during the high temperature bake [19]. It means that the overshoot current generated during activation operation, in such case, leads to a higher temperature in the active volume of the device. Consequently, a higher Ge depletion is created (i.e a lower Ge content in the active volume is achieved).

This hypothesis is in agreement with results from [15], where the surface (i.e. volume) of the Ge-depleted region is found to increase linearly with the current applied during the activation procedure. The final composition in the active volume depends on this phenomenon, leaving a material poorer in Ge and richer in Sb content, known to require a higher programming RESET current [37]. This could explain the almost absence of amorphous dome in the RESET-Fail cell, that would have required a higher RESET current to be generated than was required for the RESET-Pass device.

As Ge-rich GST materials exhibit both chemical and structure segregation at the nanoscale, an exact correlation between diffraction and EDX signals shows important benefits. Through the application of a simultaneous acquisition system for EDX and PED, coupled with hyperspectral unmixing, we outlined that a better characterisation of PCM cells can be achieved, including amorphous dome characterisation (size and composition) and GST crystalline stoichiometry determination. This new methodology could be applied to study the cycling behaviour of the PCM or to characterize the cells at different steps of the fabrication process.

Conclusion:

In this article, we studied the RESET operation in Ge-rich GST PCM devices by applying a new simultaneous acquisition system for Energy Dispersive X-ray Spectroscopy and Electron diffraction in precession mode. We highlighted the origin of the failure of the RESET operation that could happen after high temperature bake. In particular, we demonstrated the different composition (i.e. lower Ge content) achieved in the active volume of the RESET-Fail cell with respect to a standard RESET-Pass. By using VCA for hyperspectral EDX image unmixing, we detected the same GST-212 crystalline phase in both cells. However, the higher Ge-content with respect to GST-212 phase measured in the amorphous active volume of the RESET-Pass cell demonstrates the capability of the cell to feature a higher retention temperature with respect to standard GST-212, required to satisfy automotive specifications. We also evidenced that a large GST-212 grain occupies the majority of the acquisition area of RESET-Fail cell, suggesting that too much Ge has been expelled during the forming operation.

Acknowledgements:

This work, done on the NanoCharacterisation PlatForm (PFNC), was supported by the “Recherches Technologiques de Base” Program of the French Ministry of Research.

Figures

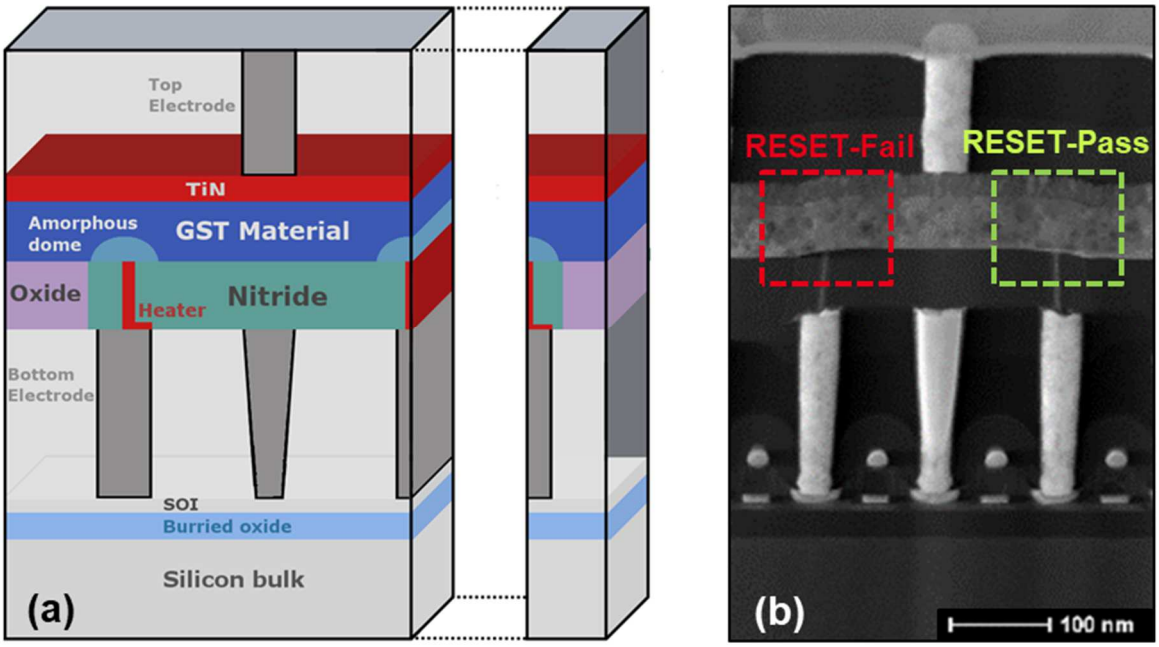

Fig. 1. (a) Schematic drawing of PCM stacking. (b) HAADF image showing the acquisition areas for the RESET-Fail (red) and the RESET-Pass (green) cells.

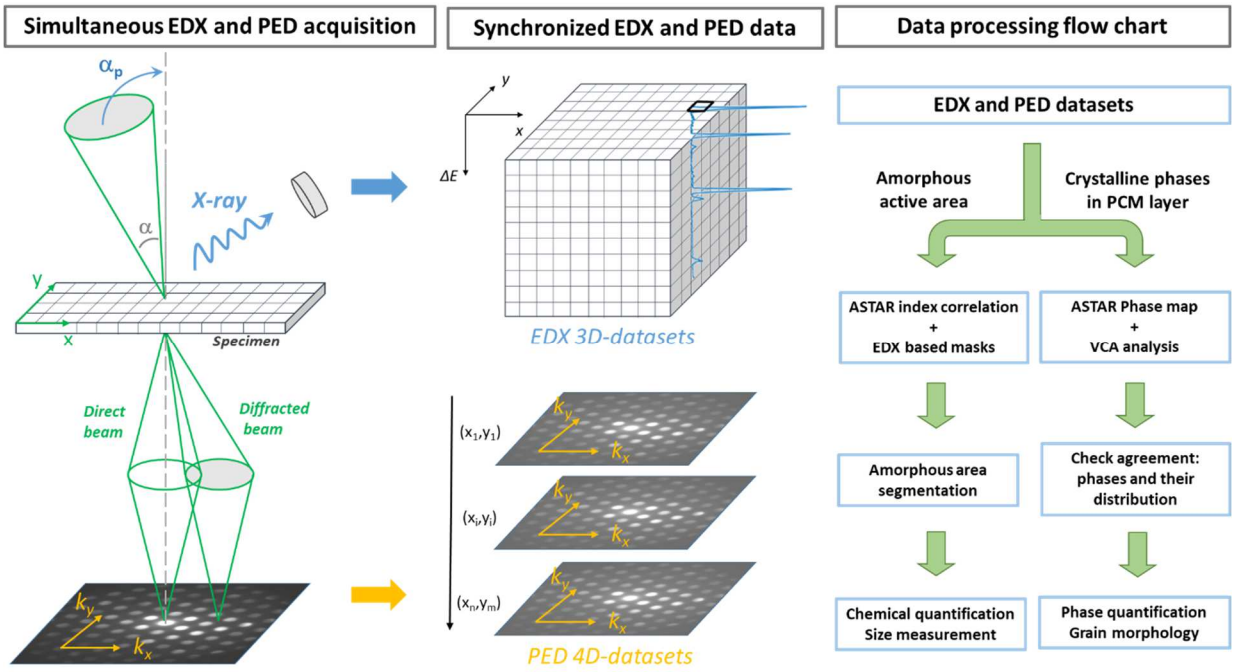

Fig. 2. Schematic of a simultaneous acquisition of PED and EDX, datasets acquired, and flow chart summarizing the main steps in data processing.

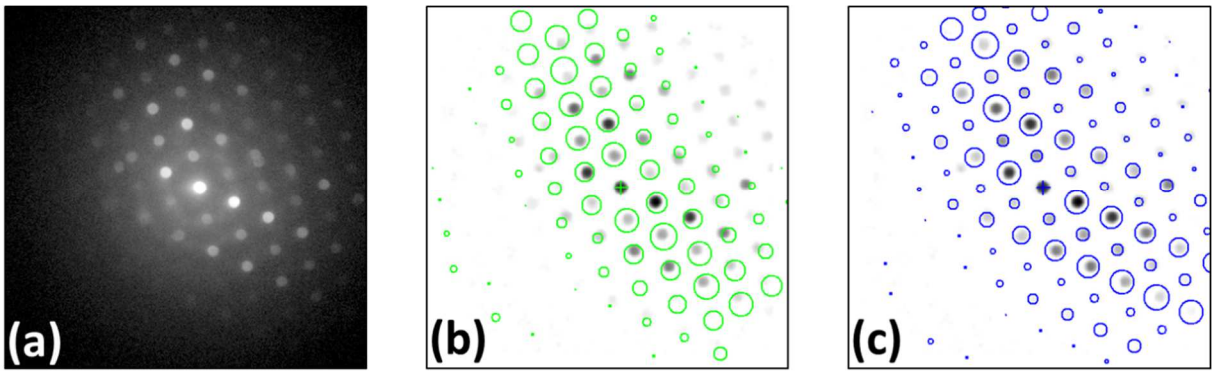

Fig. 3. (a) PED pattern acquired on the GST layer of the RESET-Fail cell and indexed either as (b) Ge (correlation index Q = 492) or (c) as $Ge_2Sb_2Te_5$ (correlation index Q = 833). In (b) and (c), the experimental PED pattern collected is compared to Ge (green) and $Ge_2Sb_2Te_5$ (blue) templates generated by ASTAR, respectively. As indicated by the higher correlation index Q and as seen in the superposition, the local crystal has not a crystal Ge structure.

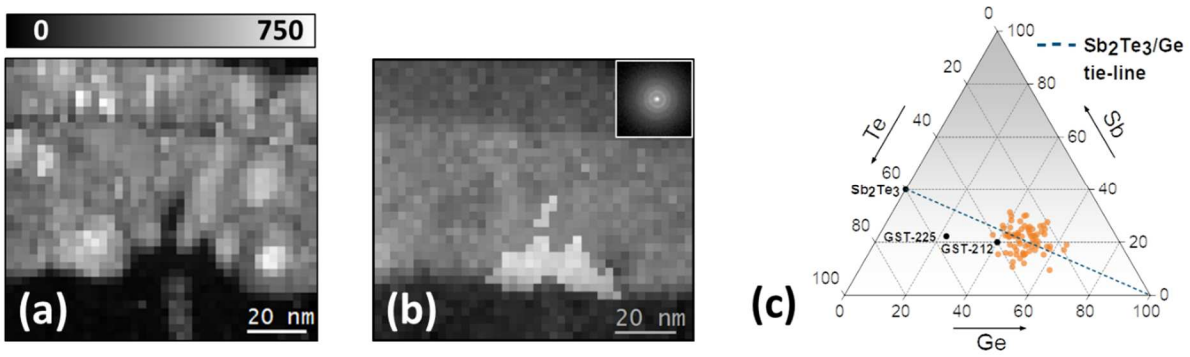

Fig. 4. (a) Index correlation map given by ASTAR software by displaying the correlation index (Q) value of each diffraction pattern acquired, (b) STEM-EDX hyperspectral image. The amorphous dome is highlighted in white by considering pixels with (i) Q <50 to distinguish amorphous from crystalline areas and (ii) a sum of Ge-K, Sb-L and Te-L X-ray net intensities higher than 30 counts to separate the GST from the surrounding layers. A typical diffraction pattern from the dome is displayed as inset. (c) Amorphous dome composition quantification results displayed in a ternary plot.

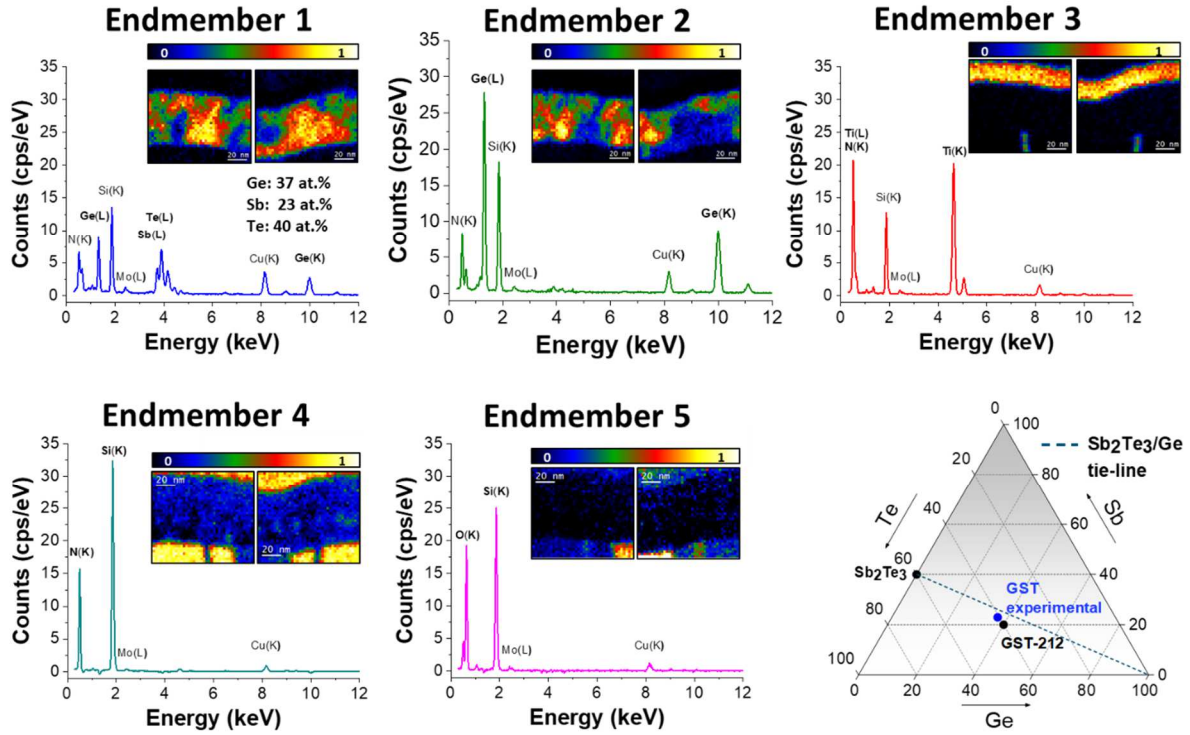

Fig. 5. Spectral components extracted by VCA. Endmembers 1 and 2 can be associated to GST and Ge phases, respectively. In order to estimate the GST phase composition displayed in the ternary plot, spectra with more than 90% of the highest abundance of GST phase were quantified. Endmembers 3 to 5 correspond to titanium nitride, silicon nitride and silicon oxide phases, respectively. The ternary plot displays both GST experimental (i.e. endmember 1) and GST-212 phases.

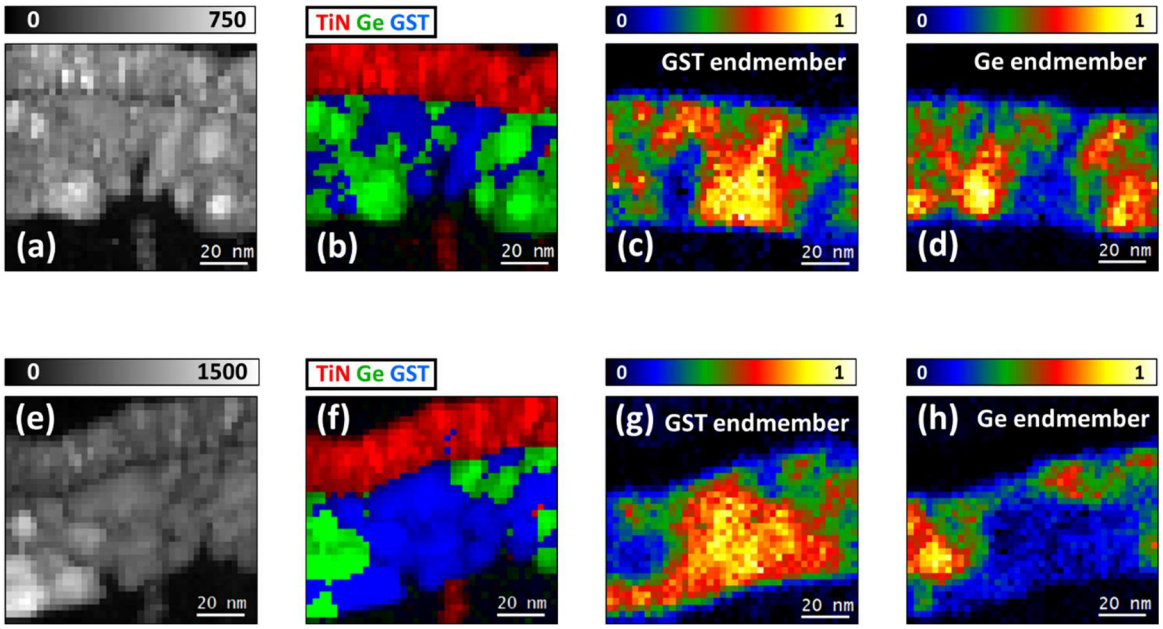

Fig. 6. (a-d) and (e-h) show results obtained on the RESET-Pass and the RESET-Fail cells, respectively. (a, e) show index correlation maps given by ASTAR software, (b, f) $Ge_2Sb_2Te_5$, Ge and TiN PED-based phase map, (c, g) and (d, h) abundance maps of the first and second spectral components extracted by VCA, respectively.

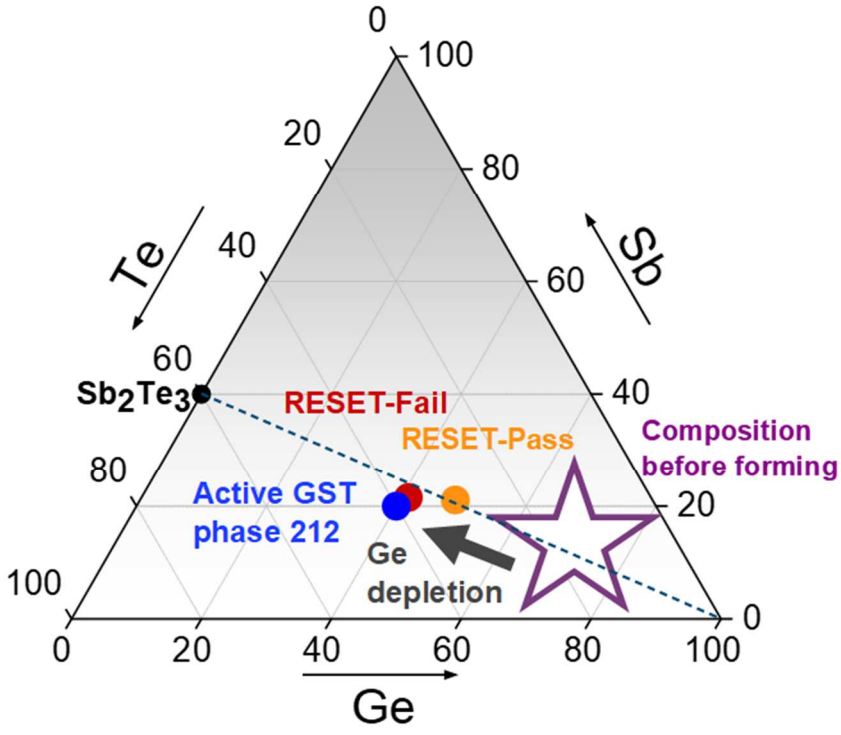

Fig. 7. Ternary plot showing the GST compositions of both RESET-Pass and RESET-Fail cells core areas. The composition of the RESET-Pass core area is calculated by taking the average of compositions measured from the amorphous dome (shown in **Fig. 3.c**). For RESET-Fail cell, we quantified EDX spectra extracted from the GST grain above the heater.

References:

[1] G.W. Burr, M.J. Breitwisch, M. Franceschini, D. Garetto, K. Gopalakrishnan, B. Jackson, B. Kurdi, C. Lam, L.A. Lastras, A. Padilla, B. Rajendran, S. Raoux, R.S. Shenoy, Phase change memory technology, J. Vac. Sci. Technol. B., 28 (2010) 223–262.

[2] R. Bez, Chalcogenide PCM: a memory technology for next decade, in: 2009 IEEE Int. Electron Devices Meet. (2009) 1-4.

[3] D. Loke, T.H. Lee, W.J. Wang, L.P. Shi, R. Zhao, Y.C. Yeo, T.C. Chong, S.R. Elliott, Breaking the Speed Limits of Phase-Change Memory, Science. 336 (2012) 1566–1569.

[4] M. Wuttig, N. Yamada, Phase-change materials for rewriteable data storage, Nat. Mater. 6.11 (2007), 824-832.

[5] H.Y. Cheng, T.H. Hsu, S. Raoux, J.Y. Wu, P.Y. Du, M. Breitwisch, Y. Zhu, E.K. Lai, E. Joseph, S. Mittal, R. Cheek, A. Schrott, S.C. Lai, H.L. Lung, C. Lam, A high performance phase change memory with fast switching speed and high temperature retention by engineering the GexSbyTezphase change material, in: 2011 Int. Electron Devices Meet. (2011) 3.4.1-3.4.4.

[6] H.Y. Cheng, J.Y. Wu, R. Cheek, S. Raoux, M. BrightSky, D. Garbin, S. Kim, T.H. Hsu, Y. Zhu, E.K. Lai, E. Joseph, A. Schrott, S.C. Lai, A. Ray, H.L. Lung, C. Lam, A thermally robust phase change memory by engineering the Ge/N concentration in (Ge, N)xSbyTezphase change material, in: 2012 Int. Electron Devices Meet. (2012) 31.1.1-31.1.4.

[7] G. Navarro, V. Sousa, P. Noe, N. Castellani, M. Coue, J. Kluge, A. Kiouseloglou, C. Sabbione, A. Persico, A. Roule, O. Cueto, S. Blonkowski, F. Fillot, N. Bernier, R. Annunziata, M. Borghi, E. Palumbo, P. Zuliani, L. Perniola, N-Doping Impact in Optimized Ge-Rich Materials Based Phase-Change Memory, in: 2016 IEEE 8th International Memory Workshop (2016) 1–4.

[8] G. Betti Beneventi, E. Gourvest, A. Fantini, L. Perniola, V. Sousa, S. Maitrejean, J.C. Bastien, A. Bastard, A. Fargeix, B. Hyot, C. Jahan, J.F. Nodin, A. Persico, D. Blachier, A. Toffoli, S. Loubriat, A. Roule, S. Lhostis, H. Feldis, G. Reimbold, T. Billon, B. De Salvo, L. Larcher, P. Pavan, D. Bensahel, P. Mazoyer, R. Annunziata, F. Boulanger, On Carbon doping to improve GeTe-based Phase-Change Memory data retention at high temperature, in: 2010 IEEE Int. Mem. Workshop (2010) 1–4.

[9] P. Zuliani, E. Varesi, E. Palumbo, M. Borghi, I. Tortorelli, D. Erbetta, G. Dalla Libera, N. Pessina, A. Gandolfo, C. Prelini, L. Ravazzi, R. Annunziata, Overcoming Temperature Limitations in Phase Change Memories With Optimized GexSbyTez, IEEE Trans. Electron Devices. 60 (2013) 4020–4026.

[10] F. Arnaud, P. Zuliani, J.P. Reynard, A. Gandolfo, F. Disegni, P. Mattavelli, E. Gomiero, G. Samanni, C. Jahan, R. Berthelon, O. Weber, E. Richard, V. Barral, A. Villaret, S. Kohler, J.C. Grenier, R. Ranica, C. Gallon, A. Souhaite, D. Ristoiu, L. Favennec, V. Caubet, S. Delmedico, N. Cherault, R. Beneyton, S. Chouteau, P.O. Sassoulas, A. Vernhet, Y.L. Friec, F. Domengie, L. Scotti, D. Pacelli, J.L. Ogier, F. Boucard, S. Lagrasta, D. Benoit, L. Clement,

P. Boivin, P. Ferreira, R. Annunziata, P. Cappelletti, Truly Innovative 28nm FDSOI Technology for Automotive Micro-Controller Applications embedding 16MB Phase Change Memory, in: 2018 IEEE Int. Electron Devices Meet. (2018) 18.4.1-18.4.4.

[11] M. Agati, M. Vallet, S. Joulié, D. Benoit, A. Claverie, Chemical phase segregation during the crystallization of Ge-rich GeSbTe alloys, J. Mater. Chem. C. 7 (2019) 8720–8729.

[12] S.M.S. Privitera, V. Sousa, C. Bongiorno, G. Navarro, C. Sabbione, E. Carria, E. Rimini, Atomic diffusion in laser irradiated Ge rich GeSbTe thin films for phase change memory applications, J. Phys. Appl. Phys. 51 (2018) 145103.

[13] S.-W. Nam, C. Kim, M.-H. Kwon, H.-S. Lee, J.-S. Wi, D. Lee, T.-Y. Lee, Y. Khang, K.-B. Kim, Phase separation behavior of Ge2Sb2Te5 line structure during electrical stress biasing, Appl. Phys. Lett. 92 (2008) 111913.

[14] V. Sousa, G. Navarro, N. Castellani, M. Coué, O. Cueto, C. Sabbione, P. Noé, L. Perniola, S. Blonkowski, P. Zuliani, R. Annunziata, Operation fundamentals in 12Mb Phase Change Memory based on innovative Ge-rich GST materials featuring high reliability performance, in: 2015 Symp. VLSI Technol. VLSI Technol. (2015) 98–99.

[15] E. Palumbo, P. Zuliani, M. Borghi, R. Annunziata, Forming operation in Ge-rich GexSbyTez phase change memories, Solid-State Electron. 133 (2017) 38-44.

[16] L. Crespi, A. Lacaita, M. Boniardi, E. Varesi, A. Ghetti, A. Redaell, G. D'Arrigo, Modeling of Atomic Migration Phenomena in Phase Change Memory Devices, in: 2015 IEEE International Memory Workshop (2015) 1-4.

[17] A. Padilla, G.W. Burr, C.T. Rettner, T. Topuria, P.M. Rice, B. Jackson, K. Virwani, A.J. Kellock, D. Dupouy, A. Debunne, R.M. Shelby, K. Gopalakrishnan, R.S. Shenoy, B.N. Kurdi, Voltage polarity effects in Ge2Sb2Te5-based phase change memory devices, J. Appl. Phys. 110 (2011) 054501.

[18] T.-Y. Yang, I.-M. Park, B.-J. Kim, Y.-C. Joo, Atomic migration in molten and crystalline Ge2Sb2Te5 under high electric field, Appl. Phys. Lett. 95 (2009) 032104.

[19] A. Valery, K. Dabertrand, R. Bon, L. Clément, Advanced TEM-based characterizations for bits fail analysis In 28 nm Phase Change Memory Test Vehicle, in: 2019 International Interconnect Technology Conference and 2019 IEEE Materials for Advanced Metallization Conference (2019), to be published.

[20] J. Kraxner, M. Schäfer, O. Röschel, G. Kothleitner, G. Haberfehlner, M. Paller, W. Grogger, Quantitative EDXS: Influence of geometry on a four detector system, Ultramicroscopy. 172 (2017) 30–39.

[21] E.F. Rauch, M. Véron, Automated crystal orientation and phase mapping in TEM, Mater. Charact. 98 (2014) 1–9.

[22] C.T. Chantler, K.J. Olsen, R.A. Dragoset, A.R. Kishore, S.A. Kotochigova, D.S. Zucker, X-Ray Form Factor, Attenuation and Scattering Tables (version 2.0), https://www.nist.gov/publications/x-ray-form-factor-attenuation-and-scattering-tables-version-20 (accessed June 6, 2019).

[23] Francisco de la Peña, Eric Prestat, Vidar Tonaas Fauske, Pierre Burdet, Petras Jokubauskas, Magnus Nord, Tom Furnival, Tomas Ostasevicius, Katherine E. MacArthur, Duncan N. Johnstone, Mike Sarahan, Jonas Lähnemann, Joshua Taillon, pquinn-dls, Vadim Migunov, Alberto Eljarrat, Thomas Aarholt, Jan Caron, Stefano Mazzucco, Ben Martineau, Suhas Somnath, Timothy Poon, Michael Walls, Tom Slater, Florian Winkler, Nicolas Tappy, Gaël Donval, Jason C. Myers, Robert McLeod, Eric R. Hoglund, hyperspy/hyperspy: HyperSpy 1.6.0, (2020).

[24] S. van der Walt, J.L. Schönberger, J. Nunez-Iglesias, F. Boulogne, J.D. Warner, N. Yager, E. Gouillart, T. Yu, scikit-image: image processing in Python, PeerJ. 2 (2014) e453.

[25] F. Pedregosa, G. Varoquaux, A. Gramfort, V. Michel, B. Thirion, O. Grisel, M. Blondel, P. Prettenhofer, R. Weiss, V. Dubourg, J. Vanderplas, A. Passos, D. Cournapeau, Scikit-learn: Machine learning in Python. J. Mach. Learn. Res. 12 (2011) 2825-2830.

[26] P. Potapov, P. Longo, E. Okunishi, Enhancement of noisy EDX HRSTEM spectrum-images by combination of filtering and PCA, Micron. 96 (2017) 29–37.

[27] J.M.P. Nascimento, J.M.B. Dias, Vertex component analysis: a fast algorithm to unmix hyperspectral data, IEEE Trans. Geosci. Remote Sens. 43 (2005) 898–910.

[28] D. Rossouw, P. Burdet, F. de la Peña, C. Ducati, B.R. Knappett, A.E.H. Wheatley, P.A. Midgley, Multicomponent Signal Unmixing from Nanoheterostructures: Overcoming the Traditional Challenges of Nanoscale X-ray Analysis via Machine Learning, Nano Lett. 15 (2015) 2716–2720.

[29] M. Shiga, K. Tatsumi, S. Muto, K. Tsuda, Y. Yamamoto, T. Mori, T. Tanji, Sparse modeling of EELS and EDX spectral imaging data by nonnegative matrix factorization, Ultramicroscopy. 170 (2016) 43–59.

[30] J.M. Bioucas-Dias, M.A.T. Figueiredo, Alternating direction algorithms for constrained sparse regression: Application to hyperspectral unmixing, in: 2010 2nd Workshop Hyperspectral Image Signal Process. Evol. Remote Sens. (2010) 1–4.

[31] A. Lagrange, https://github.com/Laadr (accessed June 6, 2019).

[32] K.-H. Kim, J.-C. Park, J.-H. Lee, J.-G. Chung, S. Heo, S.-J. Choi, Nitrogen-Doping Effect on $Ge_2Sb_2Te_5$ Chalcogenide Alloy Films during Annealing, Jpn. J. Appl. Phys 49 (2010) 101201.

[33] A.V. Crewe, J. Wall, J. Langmore, Visibility of Single Atoms, Science. 168 (1970) 1338–1340.

[34] P. Zuliani, E. Palumbo, M. Borghi, G. Dalla Libera, R. Annunziata, Engineering of chalcogenide materials for embedded applications of Phase Change Memory, Solid-State Electron. 111 (2015) 27–31.

[35] Y. Meng, J.-M. Zuo, Three-dimensional nanostructure determination from a large diffraction data set recorded using scanning electron nanodiffraction, IUCrJ. 3 (2016) 300–308.

[36] T. Bergh, D.N. Johnstone, P. Crout, S. Høgås, P.A. Midgley, R. Holmestad, P.E. Vullum, A.T.J.V. Helvoort, Nanocrystal segmentation in scanning precession electron diffraction data, J. Microsc. (2019).

[37] G. Navarro, C. Sabbione, M. Bernard, G. Bourgeois, J. Sandrini, N. Castellani, O. Cueto, J. Garrione, M.C. Cyrille, M. Frei, L. Nistor, N. Bernier, F. Fillot, E. Nolot, C. Socquet-Clerc, T. Magis, F. Laulagnet, M. Pakala, E. Nowak, Highly Sb-Rich Ge-Sb-Te Engineering in 4Kb Phase-Change Memory for High Speed and High Material Stability Under Cycling, in: 2019 IEEE 11th Int. Mem. Workshop IMW (2019) 1–4.